Effect of substituting of S for O: The sulfide perovskite $BaZrS_3$ investigated with density functional theory

Joseph W. Bennett, Ilya Grinberg, and Andrew M. Rappe
The Makineni Theoretical Laboratories, Department of Chemistry, University of Pennsylvania, Philadelphia, Pennsylvania 19104-6323, USA

(Received 17 February 2009; revised manuscript received 16 April 2009; published 9 June 2009)

We use first-principles density functional theory calculations to investigate the ground-state structure of sulfide perovskite $BaZrS_3$. The material has a lower band gap than its oxide analog $BaZrO_3$. Neither are ferroelectric in the ground state at $T=0$ K. We also examine the IR-active phonon contributions to the dielectric constant ϵ of $BaZrS_3$, which are then compared to those of $BaZrO_3$. The roles of atomic size, mass, and covalency are discussed with regard to band gap and dielectric response.

DOI: 10.1103/PhysRevB.79.235115 PACS number(s): 71.15.Mb, 77.84.−s

I. INTRODUCTION

The flexible structure of ABX_3 (X=O, S) perovskites lends itself to a variety of applications, depending upon the choice of A- and B-site atoms. It can be characterized according to the well-established tolerance factor, t, given by

$$t = \frac{R_{A-X}}{R_{B-X}\sqrt{2}}, \tag{1}$$

where R_{A-X} is the sum of A and X ionic radii and R_{B-X} is the sum of B and X ionic radii.[1] Tolerance factor $t<1$ usually leads to the rotation and expansion of the B-X_6 octahedra. Such octahedral rotations often generate a low-temperature antiferroelectric phase (e.g., $PbZrO_3$). If $t>1$, the B-X_6 octahedra are stretched from their preferred B-X bond lengths, promoting B-cation distortions by creating room for the B-cations to move off center. Therefore, simple perovskites with $t>1$ are usually ferroelectric. For example, when Pb and Ti are paired as A and B, respectively, these cations move in a concerted manner, so $PbTiO_3$ (t=1.02) is ferroelectric. Ferroelectric ABO_3 oxides are sensors in sound navigation and ranging (SONAR) devices and are also useful for nonvolatile random access memory (NVRAM) devices. When Ba and Zr are paired, the resulting oxide (t=1.00) is a dielectric with no polarization. Dielectric ABO_3 oxides are important to the wireless communication industry as components in electroceramic capacitors. Also of interest are solid solutions which contain either more than one type of A-site ($AA'BO_3$), more than one type of B-site ($ABB'O_3$), or both ($AA'BB'O_3$). While many variations in the cation composition have been intensely studied, the impact of the chemical changes on the anion site has received less attention. For example, as of yet, pairing of anion O with S in a *completely* perovskite $ABO_{3-x}S_x$ phase has not been explored.

The class of materials known as oxysulfides shows that an oxygen deficient perovskite-like phase is present as one component of a layered intergrowth phase, which is unlike the classic Ruddlesten-Popper phase of formula $AO(ABO_3)_n$. In the oxysulfide intergrowth phases, the perovskite-like layer alternates with layers of either rock salt[2] or fluorite/antifluorite phases.[3–6] To complicate matters further, the perovskite-like phase can also be found amidst both phases,[7] however in all cases, it is anion deficient.

To our knowledge, sulfide perovskites have not previously been modeled with electronic structure calculations. Sulfur analogs of perovskite oxides have been synthesized;[8–10] however many contain impurity phases that hinder studies of the pure solid, specifically the electronic structure and the dielectric properties.[11,12] In this work, we investigate the ground-state atomic structure of $BaZrS_3$, its electronic structure, and the dielectric response. We then compare these properties to $BaZrO_3$.

II. METHODOLOGY

In this study, an in-house solid state density functional theory (DFT) code, BH, employed in previous studies[13,14] is used to relax ionic positions. Lattice constants are optimized using the ABINIT software package.[15] The local-density approximation (LDA) of the exchange-correlation functional and a $4\times4\times4$ Monkhorst-Pack sampling of the Brillouin zone[16] are used for all calculations, except for the response function and Berry phase polarization calculations, for which a $6\times6\times6$ grid was used.[17] All atoms are represented by norm-conserving optimized[18] designed nonlocal[19] pseudopotentials, generated with the OPIUM code.[20] The calculations are performed with a plane-wave cutoff of 50 Ry.

Once the structure is fully relaxed, response function[21,22] calculations are performed with ABINIT to generate $D_{\alpha\beta}(i,j)$, the mass weighted dynamical matrix:

$$D_{\alpha\beta}(i,j) = \frac{\partial^2 E}{\sqrt{m_i m_j}\,\partial\,\tau_{i\alpha}\,\partial\,\tau_{j\beta}}. \tag{2}$$

where E is total DFT energy, m_i (m_j) is the mass of atom i (j), and $\tau_{i\alpha}$ ($\tau_{j\beta}$) are the displacements of atom i created in direction α (atom j in direction β). Each eigenvalue of matrix D is ν_μ^2, the frequency squared of a normalized eigenvector a_μ.

The Born effective charge tensors $Z^*_{i\alpha\beta}$ are also calculated for each atom. Each mode μ has a mode effective charge, $Z^*_{\mu\alpha}$, defined as

$$Z^*_{\mu\alpha} = \sum_{i\beta} \frac{Z^*_{i\alpha\beta}(a_\mu)_{i\beta}}{\sqrt{m_i}}, \tag{3}$$

TABLE I. Comparison of experimental (Ref. 9) and theoretical structural parameters for $BaZrS_3$. Shown first are the lattice constants along a, b, and c in Å, followed by the reduced coordinates of the atoms not located at high symmetry *Pnma* positions.

	Experiment	Theory
a	7.06	7.09
b	9.98	9.99
c	7.03	7.08
Ba(x)	0.0376	0.0517
Ba(z)	0.0069	0.0146
S1(x)	−0.0045	−0.0034
S1(z)	0.5614	0.5656
S2(x)	0.2155	0.2066
S2(y)	−0.0293	−0.0338
S2(z)	0.7869	0.7952

Contributions to the dielectric response arise only from the infrared (IR)-active modes.[23] These modes have a nonzero $Z^*_{\mu\alpha}$ and are used to calculate ϵ_μ, the contribution to the dielectric constant from mode μ (Ref. 24) as

$$\epsilon_{\mu\alpha\beta} = \frac{Z^*_{\mu\alpha} Z^*_{\mu\beta}}{4\pi^2 \epsilon_0 V \nu_\mu^2}, \tag{4}$$

where the total ionic contribution is

$$\epsilon_\mu = \frac{1}{3} \sum_\alpha \epsilon_{\mu\alpha\alpha}. \tag{5}$$

It should be noted that the quantity in Eq. (4) is the isotropic ϵ_μ averaged for a powder. Calculations are performed for a perfect crystal. The powder average is obtained by taking one-third of the trace of the dielectric tensor of the perfect single crystal.

III. RESULTS

In both $BaZrS_3$ and $BaZrO_3$ calculations, a $2\times2\times2$ supercell is used to model any possible three-dimensional perovskite tilt system.[25–27] We have shown previously that at low temperatures, the ground state of $BaZrO_3$ is not a high-symmetry $1\times1\times1$ unit cell, but a $2\times2\times2$ supercell with a Glazer tilt system $a^-b^-c^-$, or $P\bar{1}$ symmetry.[14] We find that for $BaZrS_3$ the tilt system at low temperatures is $a^-a^+a^-$ or *Pnma* symmetry, which agrees with experiment.[9] Both the lattice constants and atomic positions agree well with published data, as shown in Table I.

We find that the ground-state structure of $BaZrS_3$ is antiferroelectric (AFE), in line with expectations since $t=0.95$. This is unlike $BaZrO_3$ ($t=1.00$), for which the cation displacements are negligible, and the material exhibits paraelectric behavior at all temperatures. For $BaZrS_3$, the cations move largely in two of the three Cartesian directions, in an antiferroelectric pattern different from that of the classic $PbZrO_3$ (PZO) AFE material. In relaxed PZO, O_6 rotate into an $a^-a^-c^0$ (*Pbam* symmetry) pattern which permits concerted cation displacements along (111).[28] In $BaZrS_3$, the displacements allowed by the tilt system are better described as (101) than (111). This is because the in-phase tilts along b prevent A cations from moving along b [Fig. 1(b)], while allowing motion along a and c. The average displacements of Ba and Zr ions in $BaZrS_3$ are 0.36 and 0.07 Å, respectively. The larger Ba displacements are caused by the increased volume of its S_{12} cage, when compared to its O_{12} cage in $BaZrO_3$. The ratio of ionic radii of the anions S and O is 1.3. Such an increase in the A-site volume (relative to the size of the A cation) has been shown to give rise to large off-center distortions even for simple metal cations with no stereochemically active lone pair.[29]

The increased displacements and increased volume of $BaZrS_3$ affect the effective charges of each species as well. In $BaZrO_3$, the diagonal elements of the effective charge tensor were equal for each atom of one species, as shown in the first half of Table II. In $BaZrS_3$, however, the AFE cation displacements cause the effective charge for motion in the $\hat{x}$ and $\hat{z}$ directions to be different than the effective charge for $\hat{y}$, the direction of the smallest displacement.

Although the $Z^{*(T)}$ values of Ba are similar for $BaZrO_3$ and $BaZrS_3$, the values for Zr are increased by substituting S for O. This is due to the greater covalency of the Zr-S bonds when compared to the Zr-O bonds. The Born effective

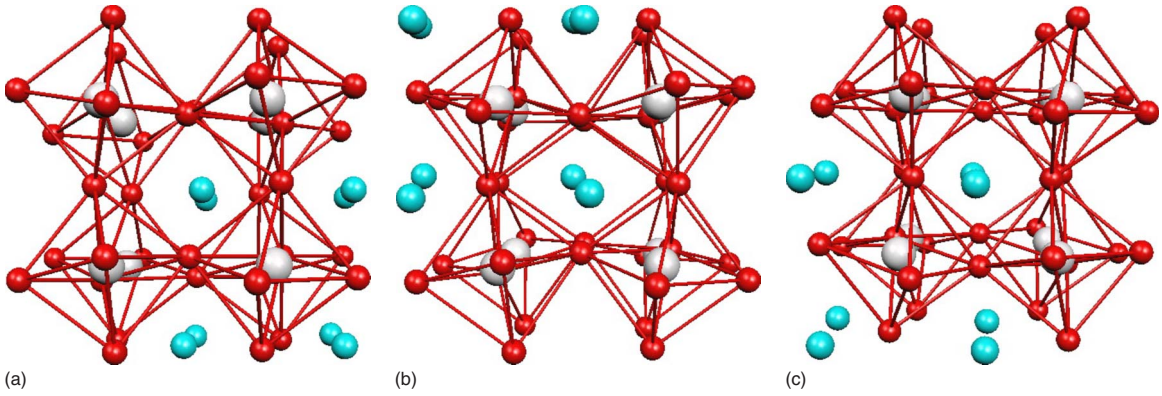

FIG. 1. (Color online) Shown here is the relaxed $2\times2\times2$ $BaZrS_3$ supercell. Ba (blue) is located at the corner of each supercell image, and Zr (gray) is inside each corner-sharing S_6 (red) octahedron. The tilt angle of S_6 cages, 12.2°, is out of phase along (a) a and (c) c, and (b) in phase along b. This indicates *Pnma* symmetry, which agrees with experiment.

TABLE II. Average diagonal values of the transverse and longitudinal effective charge tensors for each element. The longitudinal components of effective charge are the transverse components divided by ϵ_∞ and show that $BaZrS_3$ has a more covalent character than $BaZrO_3$. Shown first are values of $BaZrO_3$, then for $BaZrS_3$, which had a greater range of values for the diagonal elements.

Species	$Z^{*(T)}_{xx}$	$Z^{*(T)}_{yy}$	$Z^{*(T)}_{zz}$	$Z^{*(L)}_{xx}$	$Z^{*(L)}_{yy}$	$Z^{*(L)}_{zz}$
Ba	2.66	2.66	2.66	0.54	0.54	0.54
Zr	6.08	6.07	6.10	1.24	1.24	1.24
O1	−2.09	−2.09	−4.57	−0.43	−0.43	−0.93
O2	−2.10	−4.54	−2.10	−0.43	−0.93	−0.43
O3	−4.55	−2.10	−2.09	−0.93	−0.43	−0.43
Ba	2.81	2.92	2.81	0.29	0.30	0.29
Zr	7.22	7.56	7.20	0.75	0.79	0.75
S1	−2.44	−2.07	−5.38	−0.25	−0.22	−0.56
S2	−2.20	−6.33	−2.19	−0.23	−0.66	−0.23
S3	−5.39	−2.07	−2.44	−0.56	−0.22	−0.25

charges of the S atoms are correspondingly greater than those of the O atoms in $BaZrO_3$. An additional difference is that the highly distorted structure of $BaZrS_3$ gives rise to a range of effective anion charges, not present in $BaZrO_3$, where distortions away from high symmetry are relatively small. The effect of the increased effective charges is negated by the antiferroelectric cation displacements. This results in a decreased mode effective charge, which causes a weaker dielectric response of $BaZrS_3$ material when compared to $BaZrO_3$.

Our calculations find that the ionic part of the $BaZrS_3$ dielectric constant ϵ_μ is 20% smaller than for $BaZrO_3$, 36

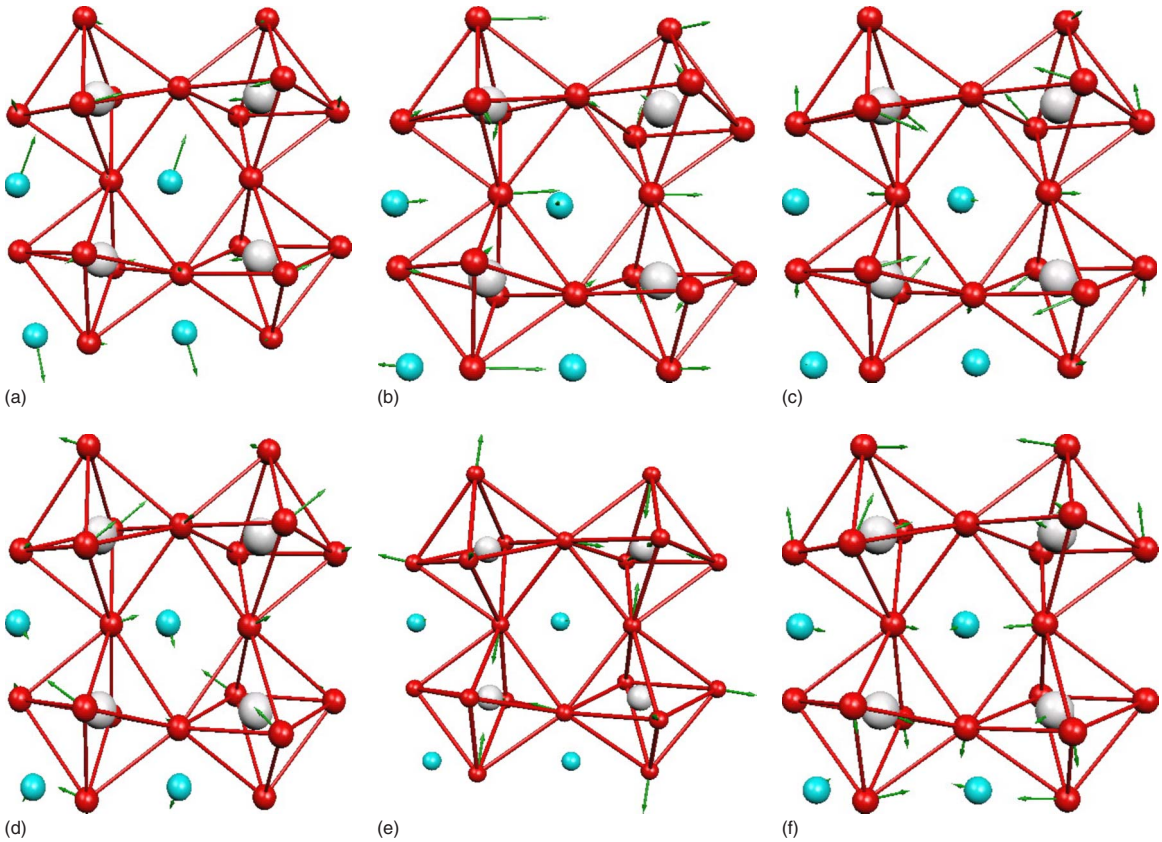

FIG. 2. (Color online) Pictured here are the three sets of $BaZrS_3$ IR-active phonon modes that contribute to ϵ. Ba (blue) is located at the corner of each supercell image, and Zr (gray) is inside each corner-sharing S_6 (red) octahedron. Green arrows indicate the direction of displacement for each normalized phonon mode. (a) shows one of the lowest-frequency modes, the Ba-S based Last modes. This mode occurs at 72 cm^{-1}. The second set, (b), (c), and (d), are Zr-S based modes that contribute the most to ϵ and occur at 116, 124, and 125 cm^{-1}, respectively. The final set, (e) and (f), are S_6 modes, which occur between 270 and 300 cm^{-1}.

TABLE III. Forty-atom low-symmetry $BaZrO_3$ phonon data for IR-active modes. Frequencies are in cm^{-1}, and mode effective charges, Z^*, are in e. The contributions to ϵ are calculated in SI units. For each IR-active mode, the atomic motions are described.

ω	Z^*_{xx}	Z^*_{yy}	Z^*_{zz}	ϵ_{xx}	ϵ_{yy}	ϵ_{zz}	Motion
106	1.3	1.3	0.5	12.1	11.7	1.9	Ba-O
107	0.5	0.5	0.2	2.0	1.9	0.3	Ba-O
114	0.4	0.4	1.8	1.0	0.8	21.8	Ba-O
125	1.2	1.3	0.0	8.5	9.0	0.0	Ba-O
184	0.2	0.3	0.1	0.1	0.2	0.0	Zr-O
192	0.3	0.7	0.0	0.3	1.1	0.0	Zr-O
195	1.3	2.3	1.0	3.6	12.2	2.2	Zr-O
196	0.3	1.0	2.7	0.2	2.0	16.3	Zr-O
197	2.5	1.3	0.2	14.1	3.5	0.1	Zr-O
211	0.6	0.6	0.0	0.7	0.6	0.0	Zr-O
307	0.2	0.1	0.6	0.1	0.0	0.3	Ba,Zr-O
308	0.4	0.4	0.2	0.2	0.1	0.1	Ba,Zr-O
501	1.5	1.9	1.2	0.8	1.2	0.5	O_6
502	0.8	0.9	2.4	0.2	0.3	1.9	O_6
505	2.1	1.7	0.0	1.4	0.9	0.0	O_6

and 45, respectively. This is mainly caused by the large increase in $BaZrS_3$ volume and smaller mode displacements, as compared to $BaZrO_3$. We observe that the frequencies of the $BaZrS_3$ phonon modes shift to lower frequencies for all motions, as expected with the heavier S atom; however, their contributions to ϵ_μ are not increased when compared to $BaZrO_3$.

The mode effective charges of $BaZrS_3$ are not as large as in $BaZrO_3$, thereby decreasing the dielectric response of the Ba-based Last modes, even at lower frequencies. This is caused by the antiferroelectric cation displacements as well as the increased covalent character of all Ba-S bonds. These two effects weaken some Ba-S bonds, which is not seen in $BaZrO_3$. The lower mode effective charges (as opposed to the Ba Born effective charge which is slightly higher in $BaZrS_3$ compared to $BaZrO_3$) are also due in part to the much larger mass of S atom (as compared to the O atom) giving smaller mode displacements. An example of the Last mode of $BaZrS_3$ is shown in Fig. 2(a). This same effect is not as drastic for the Zr-S based modes, all three of which are

TABLE IV. Same as Table III, for $BaZrS_3$

ω	Z^*_{xx}	Z^*_{yy}	Z^*_{zz}	ϵ_{xx}	ϵ_{yy}	ϵ_{zz}	Motion
54	0.0	0.4	0.0	0.0	2.6	0.0	Ba-S
58	0.0	0.3	0.0	0.0	1.3	0.0	Ba-S
72	0.8	0.0	0.5	6.5	0.0	2.3	Ba-S
75	0.3	0.0	0.0	0.9	0.0	0.0	Ba,Zr-S
81	0.5	0.0	0.3	2.0	0.0	0.9	Ba,Zr-S
86	0.4	0.0	0.4	1.0	0.0	1.0	Ba,Zr-S
116	2.4	0.0	0.5	21.7	0.0	1.0	Zr-S
118	0.3	0.5	0.0	0.4	0.8	0.0	Zr-S
124	0.4	2.1	1.2	0.4	13.6	4.8	Zr-S
125	0.6	1.2	2.0	1.0	4.8	12.3	Zr-S
140	0.0	0.8	0.0	0.0	1.8	0.0	Zr,Ba-S
141	0.0	0.8	0.0	0.0	1.6	0.0	Zr,Ba-S
153	0.7	0.0	0.4	1.0	0.0	0.3	Zr,Ba-S
159	0.7	0.0	1.0	0.9	0.0	2.0	Zr,Ba-S
218	1.1	0.0	0.9	1.1	0.0	0.9	Zr,Ba-S
270	1.8	0.0	0.8	2.2	0.0	0.4	S_6
288	1.0	0.0	2.2	0.6	0.0	2.9	S_6
293	0.0	2.4	0.0	0.0	3.4	0.0	S_6

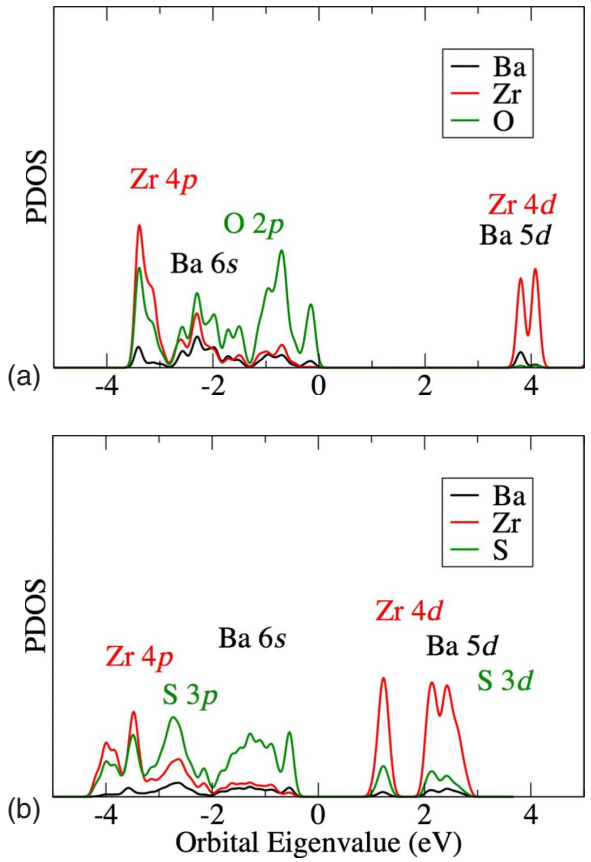

FIG. 3. (Color online) PDOS analysis shows that the electronic structure of (a) $BaZrO_3$ differs greatly from (b) $BaZrS_3$. Contributions from Ba are labeled in black, Zr in red, and O in green.

displayed in Figs. 2(b)–2(d). This could be caused by the number of bonds to S: Zr is sixfold coordinate, and Ba is 12-fold coordinate. Also, there is a larger increase in $Z^{*(T)}_{Zr}$ when comparing $BaZrS_3$ to $BaZrO_3$ than there is for $Z^{*(T)}_{Ba}$ (Table II). The S_6 modes are also left unaffected; their respective contributions are about the same as seen in $BaZrO_3$. Two of these three modes are shown in Figs. 2(e) and 2(f). The contributions of each IR active mode are tabulated first for $BaZrO_3$ in Table III and then for $BaZrS_3$ in Table IV.

Total ϵ is the sum of ϵ_∞ and ϵ_μ. The calculated ϵ_∞ of $BaZrO_3$ is 4.9 and 9.6 for $BaZrS_3$. This difference is caused by the increased covalency of Ba-S and Zr-S bonds when compared to Ba-O and Zr-O bonds, also present in the differences in the $Z^{*(L)}$ components shown in Table II. The decreased values of $Z^{*(L)}$ for the atoms in $BaZrS_3$ (when compared to $BaZrO_3$) show that the bonding in $BaZrS_3$ is more covalent in nature than the bonding in $BaZrO_3$. The calculated total ϵ of $BaZrO_3$ (50) is still slightly larger than that of $BaZrS_3$ (46).

The electronic structure of $BaZrS_3$ has been explored using an orbital-resolved projected density of states (PDOS) analysis. The DOS profile of $BaZrO_3$ [Fig. 3(a)] differs from that of $BaZrS_3$ [Fig. 3(b)]. The first major difference occurs in the region where Zr $4p$ states overlap with the anion p states, approaching the Fermi level. In $BaZrO_3$, the sharp shape of the peaks indicates a set of states that is more discrete and ionic in nature than the broader sets of more diffuse peaks present in $BaZrS_3$ in the same region. This indicates more mixing of states between Ba, Zr, and S in $BaZrS_3$ than Ba, Zr, and O in $BaZrO_3$.

What is similar in both cases is the nature of the highest occupied molecular orbital (HOMO), composed mainly of anion p states. However, in $BaZrS_3$ the lowest unoccupied molecular orbital (LUMO) is a set of states that includes some S $3d$ character, indicative of the covalent nature of the Zr-S bonds in $BaZrS_3$. This effectively lowers the energy of the LUMO. This mixing of d states does not occur in $BaZrO_3$, as O does not contain d orbitals close enough in energy to mix. These states have a lower energy in $BaZrS_3$ than in $BaZrO_3$, lowering the DFT band gap from 3.9 eV ($BaZrO_3$) to 1.7 eV ($BaZrS_3$).

IV. CONCLUSION

We have presented the first DFT study of $BaZrS_3$, including static structure relaxation, vibrational analysis, and dielectric response. We found that ϵ for $BaZrS_3$ is less than $BaZrO_3$. The larger unit-cell volume (lower atom density) of $BaZrS_3$ decreases the mode contribution of each to ϵ. Berry phase calculations show that unlike $BaZrO_3$, $BaZrS_3$ is not paraelectric, but antiferroelectric, with large displacements of Ba in $BaZrS_3$. The decrease in band gap of $BaZrS_3$ when compared to $BaZrO_3$ is driven by the mixing of unfilled S $3d$ states with empty cation d states in the LUMO.

ACKNOWLEDGMENTS

J.W.B. and A.M.R. have been supported by the Department of Energy Office of Basic Energy Sciences, under Grant No. DE-FG02-07ER46431, and I.G. by the Office of Naval Research, under Grant No. N00014-09-1-0157. Computational support was provided by U.S. DoD, by a DURIP grant, and by a Challenge Grant from the HPCMO.

[1] V. M. Goldschmidt, Naturwissenschaften **14**, 477 (1926).
[2] M. Goga, R. Seshadri, V. Ksenofontov, P. Gutlich, and W. Tremel, Chem. Commun. (Cambridge) **1999**, 979.
[3] G. Hyett, Z. A. Gal, C. F. Smura, and S. J. Clarke, Chem. Mater. **20**, 559 (2008).
[4] W. J. Zhu, P. H. Hor, A. J. Jacobson, G. Crisci, T. A. Albright, and T. Vogt, J. Am. Chem. Soc. **119**, 12398 (1997).
[5] W. J. Zhu and P. H. Hor, J. Solid State Chem. **153**, 26 (2000).
[6] K. Otzschi, H. Ogino, J. Shimoyama, and K. Kishio, J. Low Temp. Phys. **117**, 729 (1999).
[7] V. Meignen, L. Cario, A. Lafond, Y. Moelo, C. Guillot-Deudon, and A. Meerschaut, J. Solid State Chem. **177**, 2810 (2004).
[8] H. Hahn and U. Mutschke, Z. Anorg. Allg. Chem. **288**, 269 (1956).

[9] R. Lelieveld and D. J. W. Ijdo, Acta Crystallogr., Sect. B: Struct. Crystallogr. Cryst. Chem. **36**, 2223 (1980).
[10] T. Nitta, K. Nagase, and S. Hayakawa, J. Am. Ceram. Soc. **53**, 601 (1970).
[11] Y. Wang, N. Sato, K. Yamada, and T. Fujino, J. Alloys Compd. **311**, 214 (2000).
[12] Y. Wang, N. Sato, and T. Fujino, J. Alloys Compd. **327**, 104 (2001).
[13] S. E. Mason, I. Grinberg, and A. M. Rappe, Phys. Rev. B **69**, 161401(R) (2004).
[14] J. W. Bennett, I. Grinberg, and A. M. Rappe, Phys. Rev. B **73**, 180102(R) (2006).
[15] X. Gonze *et al.*, Comput. Mater. Sci. **25**, 478 (2002).
[16] H. J. Monkhorst and J. D. Pack, Phys. Rev. B **13**, 5188 (1976).
[17] R. Resta, Rev. Mod. Phys. **66**, 899 (1994).
[18] A. M. Rappe, K. M. Rabe, E. Kaxiras, and J. D. Joannopoulos, Phys. Rev. B **41**, 1227(R) (1990).
[19] N. J. Ramer and A. M. Rappe, Phys. Rev. B **59**, 12471 (1999).
[20] http://opium.sourceforge.net
[21] X. Gonze and C. Lee, Phys. Rev. B **55**, 10355 (1997).
[22] P. Ghosez, J.-P. Michenaud, and X. Gonze, Phys. Rev. B **58**, 6224 (1998).
[23] E. Cockayne and B. P. Burton, Phys. Rev. B **62**, 3735 (2000).
[24] E. Cockayne, J. Eur. Ceram. Soc. **23**, 2375 (2003).
[25] A. M. Glazer, Acta Crystallogr. **B28**, 3384 (1972).
[26] P. M. Woodward, Acta Crystallogr., Sect. B: Struct. Sci. **53**, 32 (1997).
[27] P. M. Woodward, Acta Crystallogr., Sect. B: Struct. Sci. **53**, 44 (1997).
[28] D. J. Singh, Phys. Rev. B **52**, 12559 (1995).
[29] R. Kagimura, M. Suewattana, and D. J. Singh, Phys. Rev. B **78**, 012103 (2008).